Upscaling high activity oxygen evolution catalysts based on CoFe2O4 nanoparticles supported on nickel foam for power-to-gas electrochemical conversion with energy efficiencies above 80%.

Félix Urbain[1], Ruifeng Du[1], Pengyi Tang[1,2], Vladimir Smirnov[3], Teresa Andreu[1,4], Friedhelm Finger[3], Jordi Arbiol[2,5], Andreu Cabot[1,5], and Joan Ramon Morante[1,6]*

[1] IREC, Catalonia Institute for Energy Research, Jardins de les Dones de Negre 1, 08930 Sant Adrià de Besòs, Barcelona, Catalonia, Spain

[2] Catalan Institute of Nanoscience and Nanotechnology (ICN2), CSIC and BIST, Campus UAB, Bellaterra, 08193 Barcelona, Catalonia, Spain

[3] IEK-5 Photovoltaik, Forschungszentrum Jülich, D-52425, Jülich, Germany

[4] Universitat Politècnica de Catalunya, Jordi Girona 1–3, 08034 Barcelona, Catalonia, Spain

[5] ICREA, Pg. Lluís Companys 23, 08010 Barcelona, Catalonia, Spain

[6] Universitat de Barcelona, Martí i Franquès, 1, 08028 Barcelona, Catalonia, Spain

[*] **Corresponding Author**: E-Mail: furbain@irec.cat

Abstract

Water electrolysis, which is a key technology to push forward the energy turnaround, necessitates efficient approaches for the fabrication of cost-effective and highly active electrodes for the oxygen evolution reaction (OER) at large scale. Here we report on the development of a scalable process for the synthesis and loading of highly active $CoFe_2O_4$ ferrite nanoparticles (< 10 nm) on low-cost and high surface area electrodes. Three-dimensional (3D) nickel foam (NF) was used as scaffold material and the $CoFe_2O_4$ coating process was adapted for large-area electrodes regarding scalability, particle size and distribution. The combination of the optimized $CoFe_2O_4$ nanoparticles coated on the 3D NF scaffold resulted in superior OER performance with low overpotential, high current density, and long-term durability in alkaline solution, outperforming the single component counterparts. Impressively, the overpotential at currents of 500 mA did not surpass 300 mV with geometric surface area of 10 cm^2 of the $CoFe_2O_4$ coated NF electrode. The integration in a prototype water electrolyzer, that applied a Pt-coated Ti plate as cathode and a bipolar membrane to separate anolyte (alkaline) and catholyte (acid) compartments, manifested stable operating currents of 500 mA at impressively low cell-voltages of 1.62 and 1.53 V, respectively, at ambient and elevated electrolyte temperatures, respectively. Coupled to a low-cost thin-film silicon solar cell, bias-free solar water splitting was furthermore demonstrated, affording a high solar-to-fuel efficiency of over 10 %. In total, the present work outlines the important steps toward the exploration of cost-effective and efficient OER electrocatalysts, able to substitute noble metals for commercially relevant renewable energy conversion/storage applications.

1. Introduction

A major technology to propel the energy transition is water electrolysis for hydrogen (H_2) production, which thanks to tremendous engineering and scientific efforts has been successfully brought to market maturity.[1] At present, the industrial breakthrough is, however, still hampered due to the high costs of noble metal catalysts and the low energy conversion efficiency, particularly for the water oxidation reaction. The latter half reaction of the water splitting reaction is called oxygen evolution reaction (OER) and is kinetically more difficult to occur than the concomitant hydrogen evolution reaction (HER), mainly due to strong oxygen double bond formation and the multi-electron transfer step arising thereby.[2] In order to enhance the OER performance, most large-scale electrolyzer systems therefore utilize expensive benchmarking OER catalyst materials, such as IrO_2 or RuO_2.[3] As a consequence, there is the dilemma for commercial electrolyzers of either being too costly or too inefficient, because more cost-effective systems, employing non-precious catalysts, suffer from unpractical high overpotential losses to provide commercially satisfactory currents (> 200 mA) and thus, are not competitive with alternative H_2 production pathways.[4-6] Nevertheless, on laboratory scale promising examples on high current water electrolysis below 1.6 V operating voltage have been demonstrated applying non-noble OER catalyst materials, such as transition metal oxides and hydroxides [7,8]. For the most part however, these studies are either limited to small-scale electrodes or energy-intensive deposition methods and consequently lack of the scalability feature, which is crucial for any kind of commercial application. Against this backdrop, the present study is dedicated toward the realization of a prototype electrolyzer utilizing a scalable process for the synthesis and coating of high-performing and environmentally friendly OER catalysts on large-scale electrode scaffolds.

Among non-noble OER catalyst materials, spinel-type binary transition metal oxides (AB_2O_4, A, B = metal) come to the fore, which besides their high abundance and low toxicity, have proven to be conducive to a rich redox chemistry and chemical robustness.[9-11] In particular, the activity of bimetallic Co-Fe spinel compounds towards water oxidation has been extensively investigated.[12-18] Bimetallic catalysts offer additional degrees of freedom compared to elemental compositions, enabling more optimum active sites for the associated OER catalysis steps and in its oxidized form they additionally offer high electrochemical stability. Oxide structures, however, suffer from intrinsically inferior electrical conductivity. To circumvent this issue for the $CoFe_2O_4$ catalysts, we aimed to synthesize the particles in the low nanometer range (< 10 nm) and attach them to a highly conductive scaffold material, such as nickel (Ni) foam and thus, facilitating the charge transfer of the conjoint OER system.

Related studies on $CoFe_2O_4$ particles loaded on high surface area scaffolds, such as doped carbon nanofibers [15] or hematite nanorods [19], are limited to laboratory-scale applications, mainly due to the complexity and high cost of the utilized synthesis routes, such as micro emulsion[20] and hydrothermal[13], respectively. Herein, we therefore firstly developed a cheap and scalable synthesis method for $CoFe_2O_4$ ferrite nanoparticles (NPs) for efficient OER and secondly, optimized the loading of the earth-abundant and active NPs on large-scale Ni foam (NF), as highly conductive, three-dimensional (3D) and cost-effective electrode scaffold. We provide evidence that the applied colloidal synthesis for the $CoFe_2O_4$ NPs bears great benefits regarding scalable preparation and loading on Ni foam, such that optimum size and distribution for low-overpotential OER can be achieved. Following the optimization of the coating process, the $CoFe_2O_4$ coated Ni foam electrode (denoted as $CoFe_2O_4$@NF hereafter) was tested in a prototype electrolysis system to assess the viability for high yield H_2 production. Our results show that the

synergy between the high OER catalytic activity of the $CoFe_2O_4$ paired with the high surface area of the supporting large-scale Ni foam were conducive to excellent overall water splitting, achieving cell voltages of 1.62 V and 1.53 V at currents of 500 mA for ambient and elevated temperature operation, respectively. Furthermore, we assessed the versatility of the presented system for different power sources by coupling the electrolyzer to a thin-film silicon solar cell for bias-free solar water splitting, achieving a solar-to-hydrogen efficiency of 10.03 %.
In total, the presented results set a new benchmark performance for transition metal oxides anchored on large-scale electrode support for the OER and thus, may help to push the frontier of the field of environmentally friendly processes and electrodes for commercially viable water electrolysis.

2. Results

2.1. Synthesis and Characterization of Colloidal $CoFe_2O_4$ NPs

Colloidal $CoFe_2O_4$ ferrite NPs were synthesized from the reduction of appropriate amounts of cobalt and iron salts in the presence of OAm and OAc (see the Experimental Section for details). Scheme 1 illustrates the preparation procedure for NP synthesis at 230ºC. The representative transmission electron microscopy (TEM) micrograph and size distribution of the as-prepared NPs, respectively, are shown in Figure 1a. An average size for the quasi-spherical $CoFe_2O_4$ particles of 7.1 ± 0.05 nm was deduced from the TEM image in Figure 1a.

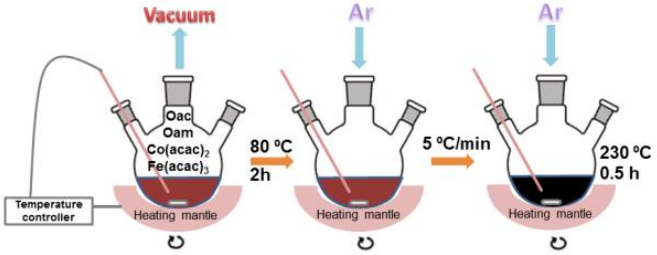

Scheme 1. Schematic illustration of the synthesis procedure to prepare colloidal $CoFe_2O_4$ NPs.

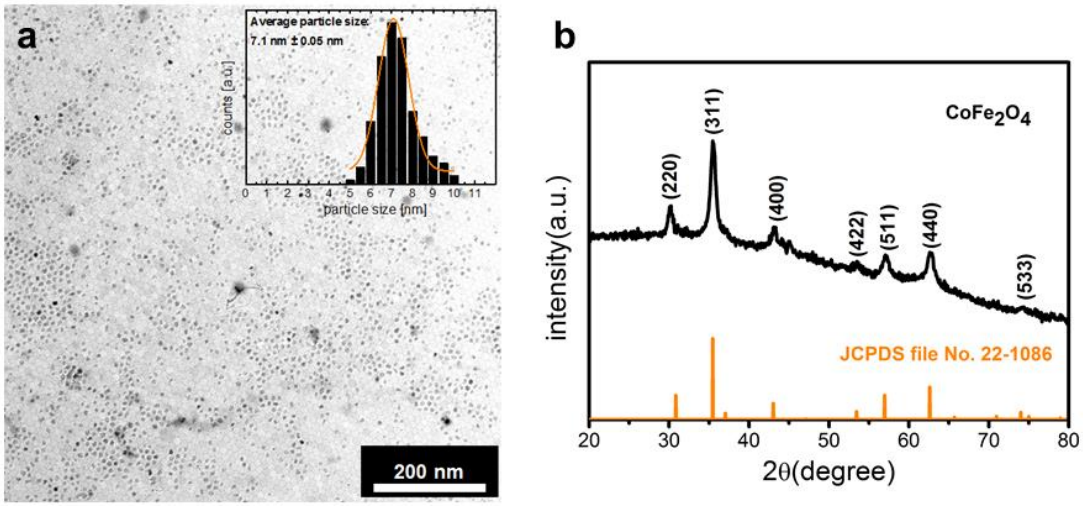

Figure 1. a) Representative TEM micrograph of $CoFe_2O_4$ NPs. Scale bar: 200 nm. Inset: Histogram showing the size distribution of the as-prepared NPs obtained from the TEM image

with an average particle size of 7.1 ± 0.05 nm. b) XRD pattern of the as-prepared NPs showing the signals stemming from cubic phase of $CoFe_2O_4$ (JCPDS card number 22-1086*).*

The crystalline structure of the as-deposited NPs was investigated by X-ray diffraction (XRD) and the corresponding diffraction pattern is shown in Figure 1b. The analysis revealed that the $CoFe_2O_4$ catalyst particles crystallized in the cubic phase as all the diffraction peaks are indexed to a pure cubic phase (*JCPDS card number 22-1086)* of $CoFe_2O_4$, as indicated in Figure 1b. Based on the annular dark-field (ADF)-scanning (S)TEM image in Figure 2a, electron energy loss spectroscopy (EELS) analysis was conducted for the NPs evidencing that the three elements Co, Fe, and O were found homogeneously distributed as shown in the composition maps of single NPs (Figure 2a). From the high resolution (HR)TEM micrograph in Figure 2b (detail view in Figure 2c), the crystal structure of the NPs could be determined by the fast Fourier transform (FFT) spectrum (Figure 2d) and was compatible with that of the $CoFe_2O_4$ ferrite cubic phase ([FM3-MZ]-Space group) with lattice parameters of a = b = c = 0.83961 nm. A complementary HRTEM characterization of the $CoFe_2O_4$ NP is presented in the Supporting Information (SI) in Figure S1, revealing its crystalline structure.

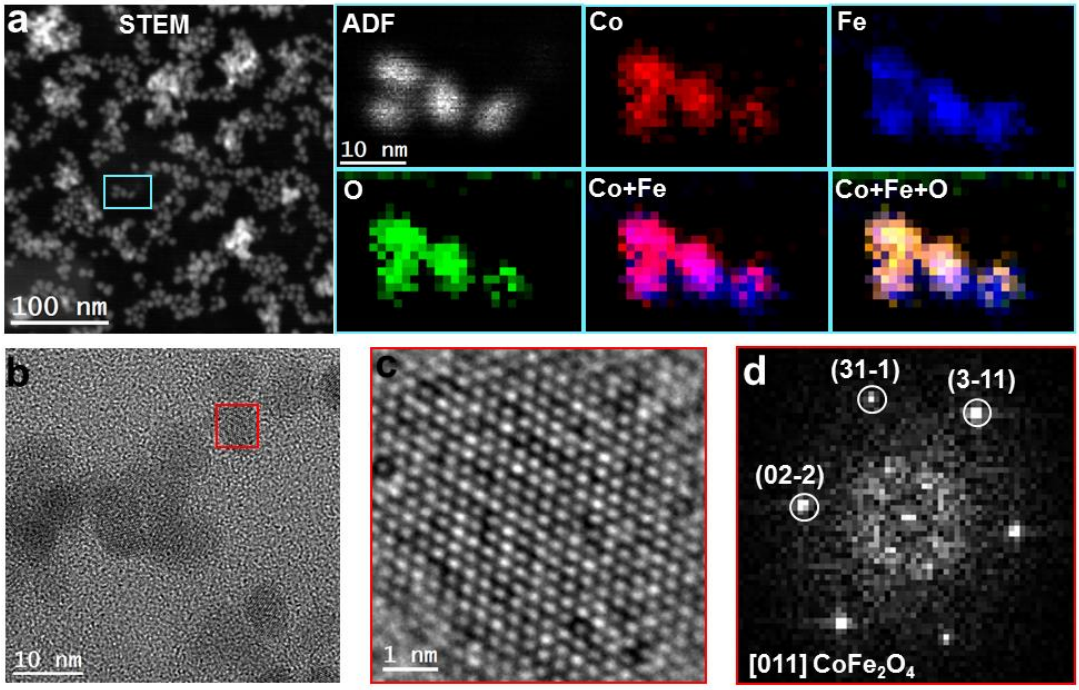

Figure 2. a) ADF-STEM micrograph (scale bar, 100 nm) and the corresponding EELS chemical composition maps for the individual Co (red), Fe (blue), O (green) and their composites, obtained from the cyan rectangled area of the STEM image (scale bar, 10 nm). b) HRTEM image showing the structure of the nanoparticles (scale bar, 10 nm). c) HRTEM detail of the red squared region (scale bar, 1 nm). d) Corresponding FFT spectrum indicating that the material crystallizes in the cubic $CoFe_2O_4$ phase, [FM3-MZ]-Space group 227, with lattice parameters of a = b = c = 0.83961 nm, and $\alpha = \beta = \gamma = 90°$as visualized along the [011] direction.

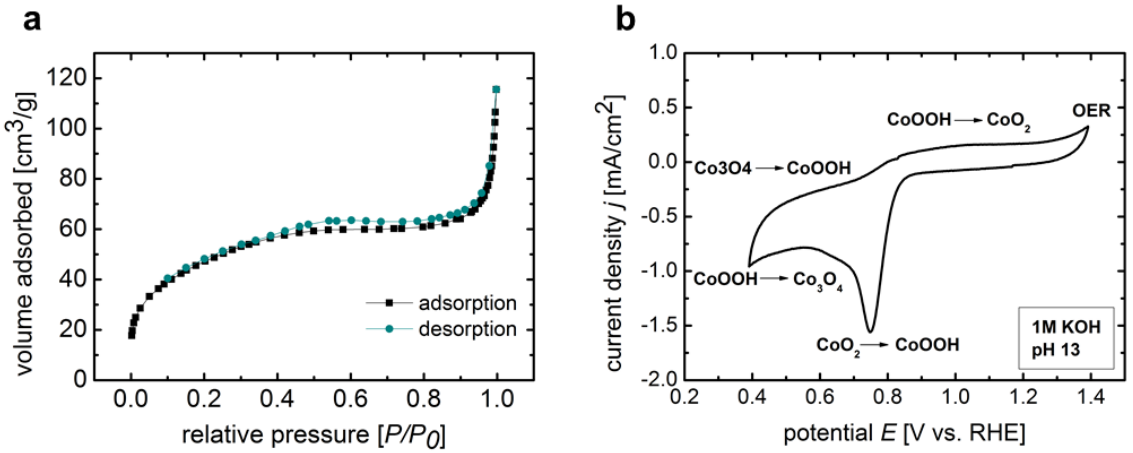

Figure 3. a) N_2 adsorption–desorption isotherms. b) Rotating disk electrode CV measurement of the as-produced $CoFe_2O_4$ nanoparticles in 1M KOH at a scan rate of 10 mV/s. The tentative reduction and oxidation products are assigned.

N_2 sorption experiments were performed to examine the specific surface area of the $CoFe_2O_4$ NPs. The corresponding N_2 adsorption–desorption isotherms, shown in Figure 3a, can be categorized as type-I isotherms with a reversible behavior and limiting values at pressure ratios P/P_0 ~ 1. Such a behavior generally results from microporous solids having small external surface areas with pore widths in the range of 0.7-2 nm.[21] The analyzed samples yielded a Langmuir specific surface area (SSA) of 276.3 m^2/g and a Brunauer–Emmett–Teller (BET) SSA of 174.0 m^2/g. The obtained BET value is among the highest reported for Co-Fe spinel compound NP catalysts, being in good agreement with NPs synthesized by hydrothermal[13] and micro emulsion technique[20] (~150 m^2/g), respectively, and significantly higher than Co-Fe compound NPs prepared by electrospinning[15] and electrodeposition,[16] respectively (~55 m^2/g). This result evidences that the colloidal synthesis route perfectly fulfils the requirements regarding the preparation of high surface area Co-Fe compound particles.

The electrochemical behavior of the as-produced $CoFe_2O_4$ NPs was investigated in a glassy carbon electrode configuration and is presented in Figure 3b for the potential range of 0.4 - 1.4 V_{RHE}. In an alkaline medium, Co is generally found in an oxidized form [22,23] and the cyclic voltammetry (CV) measurement in Figure 3b shows the corresponding successive oxidation and reduction between cobalt oxide, hydroxide and/or oxyhydroxide phases. During the forward scan, at 0.5 V_{RHE}, cobalt further oxidized probably to CoOOH and at ca. 1.0 V_{RHE}, CoOOH further oxidized, possibly to CoO_2.[24,25] Both phases were then reduced during the reverse scan. Nevertheless, the $CoFe_2O_4$ NPs were found to be active toward the OER, as water oxidation started at low potentials ~ 1.4 V_{RHE} (Figure 3b). To enhance the performance of the OER electrode, the subsequent step consisted in attaching the active $CoFe_2O_4$ NPs on a 3D conductive and cost-effective scaffold electrode, namely Ni foam.

2.2. Loading on Large-scale Ni Foam

The coating of the nano-sized OER catalysts onto large-scale scaffold materials is an important step toward the realization of industry-viable electrodes and electrolyzers. For this purpose, we first studied the deposition of the NPs on small (1 cm^2) Ni foam electrodes and subsequently optimized the deposition process for larger scaffold areas (≥10 cm^2). Before the deposition, the organic ligands at the surface of the as-synthesized NP, which were used during the synthesis, needed to be removed. In general, organic ligands strongly limit the electronic interaction and the ability of the NPs to interact with

their surrounding media, i.e. with the scaffold and the electrolyte.[26] Furthermore, in our case, the presence of organic ligands particularly impeded a homogeneous coating of the Ni foam with the $CoFe_2O_4$ NPs. As observable from Figure S2 in the SI, a porous two-dimensional carbon film was deposited on the Ni foam after dip coating into the NP containing suspension, preventing the NPs to attach to the scaffold surface. The removal of the organic ligands from the surface of $CoFe_2O_4$ NPs was conducted in a solution containing 1 M hydrazine hydrate in acetonitrile (see Experimental Section). After successive cleaning with tetrafluoroboric acid, the Fourier transform infrared spectroscopy (FTIR) spectra in Figure S3 shows the disappearance of the peaks at 2822 and 2890 cm^{-1}, respectively, corresponding to C–H stretching modes, evidencing the effective ligand removal.

Figure 4a illustrates the two tested coating procedures applied for immobilizing the $CoFe_2O_4$ NPs on the NF samples: dip coating and drop casting. As depicted, the foam was either dipped into the NP containing suspension (and hold for 2 seconds) or the suspension was dropped onto the foam (2 mg of solution). The SEM images in Figure 4a show that the dip coating was conducive to a homogeneous distribution of the NPs on the Ni foam surface, whereas the drop casting technique resulted in bigger agglomerated particle structures. The electrochemical performance of both prepared electrodes toward the OER is shown in Figure 4b. In comparison with bare Ni foam, used in industrial water splitting, both $CoFe_2O_4$@NF electrodes significantly enhanced the OER, highlighting the synergetic effect between $CoFe_2O_4$ and the 3D NF scaffold. As apparent from Figure 4c, the two $CoFe_2O_4$ containing NFs (dip coating and drop casting) can provide much higher current densities under the same applied potential than the bare NF. For all investigated potentials the $CoFe_2O_4$ containing NFs exhibited 2 to nearly 4 times higher current densities. In addition, Figure 4b and 4c also evidence the superior characteristics of the $CoFe_2O_4$@NF prepared by dip coating compared with the electrode prepared by drop casting. Based on the SEM images shown in Figure 4a, this result could be expected as it is known that thinly dispersed oxide nanoparticles favor the electrochemical performance.[27] A significant increase in the current density for potentials > 1.5 V was measured for the sample prepared by dip coating, attaining 43.8 mA/cm^2 at 1.7 V_{RHE} (470 mV overpotential), which is 1.4 times higher than that obtained with the drop casted sample.

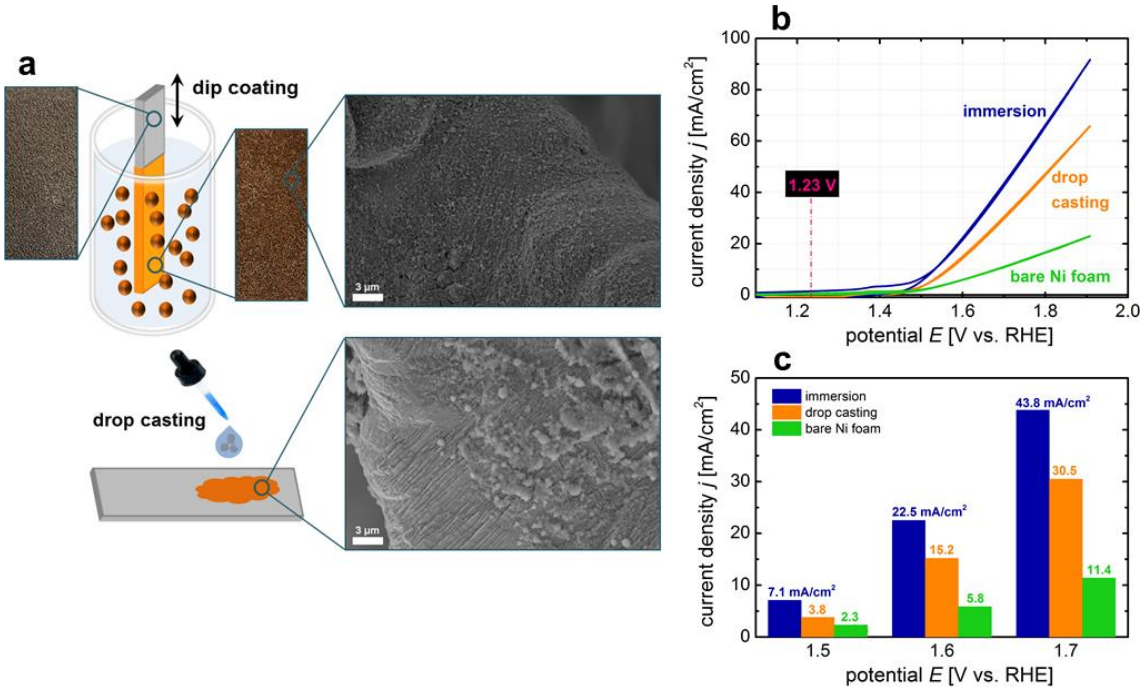

Figure 4. a) Schematic illustration of the two tested coating techniques for the $CoFe_2O_4$ on the Ni foam (1 cm^2 geometric area): dip coating and drop-casting, including photographs of the Ni foam before and after the coating processes, as well as SEM images showing the distribution of the deposited particle on the Ni foam surface. b) CV curves of the Ni foam coated with $CoFe_2O_4$ NPs by dip coating and drop casting, respectively, compared with bare Ni foam. Measurements were conducted in 1 M KOH at a scan rate of 10 mV/s. c) Current densities achieved at different applied potentials.

The dip coating technique was further optimized for large area electrodes (10 cm^2) by investigating how the dipping into the NP suspension affects the coating. Figure 5 presents the SEM images of the NF surfaces after 1, 3, 5, and 7 dips (each hold for 2 seconds) into the $CoFe_2O_4$ suspension. After 1 dip major parts of the NF remained uncovered, whereas 3 dips resulted in much better coverage of the NF surface with highly dispersed NPs in the range of 5 - 10 nm. Figure S4 in the SI, shows a photograph of the NF sample before and after 3 dips. Increasing the dipping time to 5 dips, led to bigger agglomerated particles, ranging from 50 to 200 nm in size, as can be deduced from Figure 5. This effect was even more pronounced after 7 dipping times, resulting in an almost complete coverage of the NF surface by $CoFe_2O_4$ agglomerates.

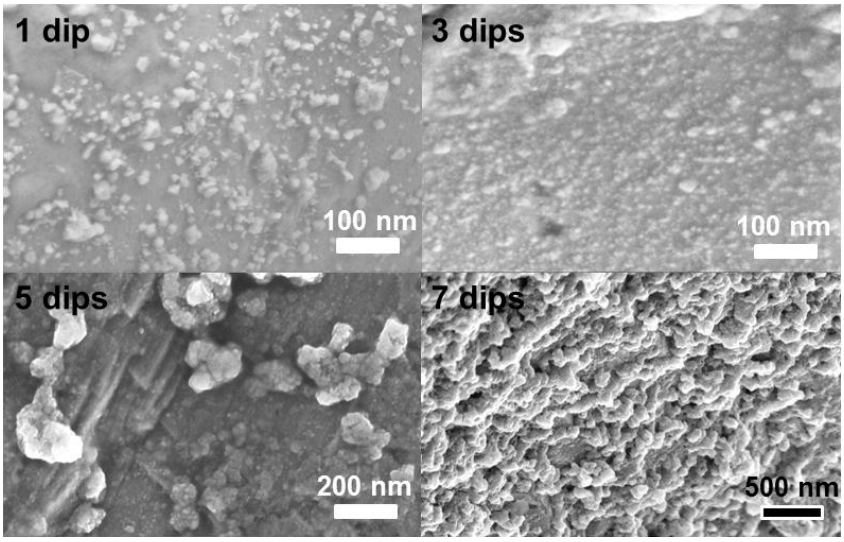

Figure 5. SEM analysis of the $CoFe_2O_4$ NP coating on the Ni foam (10 cm^2) depending on the number of dips into the NP containing solution. Dipping times of 1,3,5, and 7 times were tested.

The electrochemical characteristics of the large-scale $CoFe_2O_4$@NF electrodes were assessed in a three-electrode configuration using 1M KOH electrolyte solution (see Experimental Section). Figure 6a shows the CV curves of the electrode samples investigated in Figure 5. It can be seen that the dipping time has a significant effect on the OER, as could be expected from the SEM analysis. The best performance was achieved with the $CoFe_2O_4$@NF electrode which was dipped 3 times into the NP suspension, being in good agreement with the results from Figure 5, as 3 dipping times provided the best homogeneous coverage of the NF surface with thinly dispersed NPs. The OER overpotentials of the four tested samples for different current densities are shown in Figure 6b, evidencing that the 3 times dipped electrode exhibited the lowest overpotentials, with 250 mV and 460 mV for 10 mA/cm^2 and 50 mA/cm^2, respectively. The electrodes owing the agglomerated particles, observable in Figure 5 for 5 and 7 dips, respectively, slightly impaired the OER performance. This result is understandable as oxide structures in general suffer high electrical resistivity, which is even more pronounced if the particle size is increased. The highest overpotential of 580 mV at 50 mA/cm^2, was measured for the 1 time dipped electrode, presumably due to an insufficient coverage of the scaffold by the $CoFe_2O_4$ NPs (see Figure 5).

Commercial alkaline electrolyzers work at operating temperature between 25 and 100 ºC, which is why we tested the best performing electrode (3 dips) also under elevated electrolyte temperature. As apparent from Figure 6a and 6b, the OER performance was significantly enhanced by increasing the electrolyte temperature up to 50 ºC, mainly due to enhanced electrochemical kinetics. Extremely low overpotentials of 210 mV and 295 mV for 10 mA/cm^2 and 50 mA/cm^2, respectively were obtained. Such values can be found among the best state-of-the-art OER electrodes in literature, evidencing the high potential for commercial applications of the herein developed large-scale $CoFe_2O_4$@NF OER electrodes. State-of-the-art electrocatalytic properties toward OER of previously reported Co-Fe or Ni foam based electrodes are summarized in Table S1 in the SI.

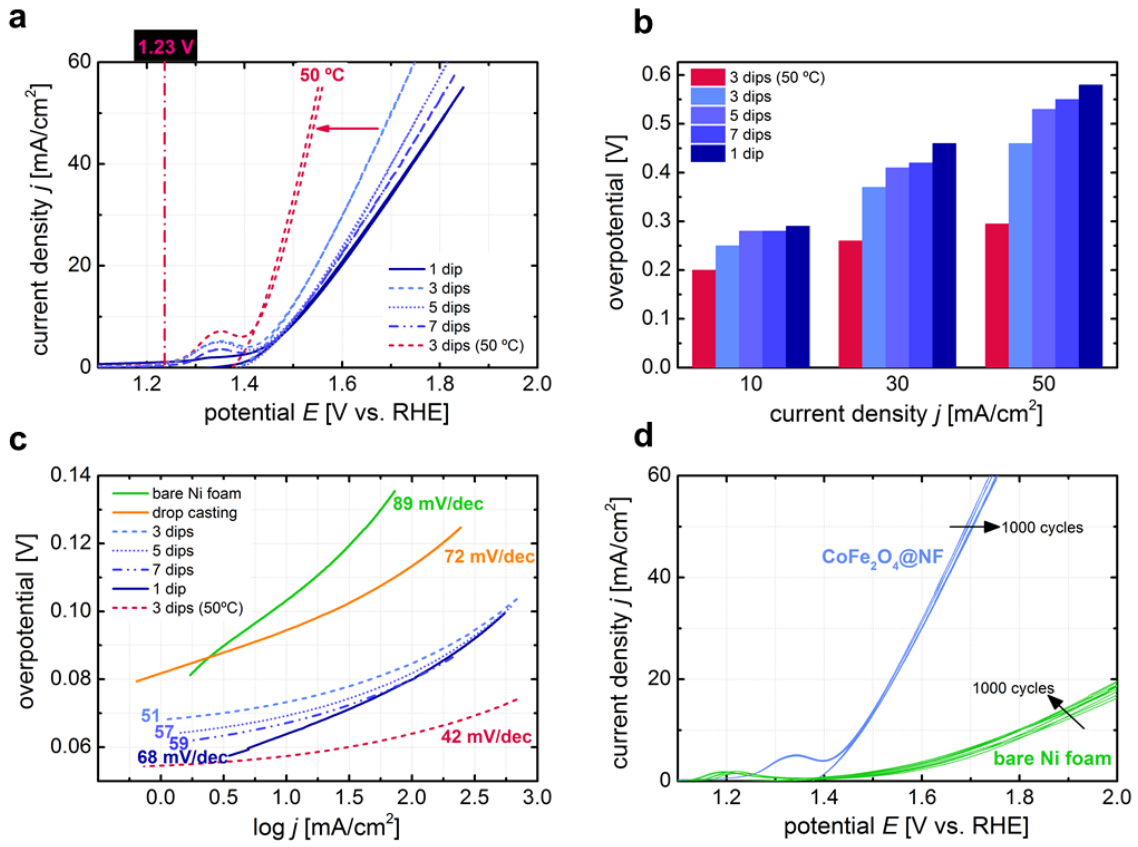

Figure 6. a) CV curves of NF electrodes dipped into the $CoFe_2O_4$ containing solution, for 1 (solid), 3 (dashed), 5 (dotted), and 7 (dash-dotted) times. The curves were measured in 1M KOH at a scan rate of 10 mV/s. The best performing OER sample (3 dips) was measured under elevated electrolyte temperature (50 °C, pink dashed line). The H_2O/O_2 oxidation potential is indicated by the straight dash-dotted line. b) Required overpotentials derived from the CV curves in a) at different current densities. c) Tafel plots of the samples tested in a). d) CV curves of the $CoFe_2O_4$@NF (3 dips) and bare Ni foam electrodes, respectively, before and after 1000 cycles. Every 200th CV scan is plotted for both electrodes.

The electrocatalytic kinetics for OER of the $CoFe_2O_4$@NF electrodes were further investigated by Tafel plots, as displayed in Figure 6c. For comparison, the Tafel plots of the sample prepared by drop casting and the bare Ni foam sample are also shown in Figure 6c. In accordance to the results shown in Figure 4b and 4c, respectively, these two electrodes exhibited the worst kinetics among the analyzed electrodes, i.e. the highest Tafel slopes of 89 and 72 mV/dec, respectively. For the $CoFe_2O_4$@NF electrodes prepared by dip coating, the Tafel slopes are impressively low and ranged from 68 mV/dec for the 1 time dipped sample to 51 mV/dec for the 3 times dipped electrode. Hence, as compared with related nonprecious metal-based OER electrocatalysts reported in literature, our $CoFe_2O_4$@NF show comparable and even better electrocatalytic properties toward OER (Table S1 of the SI). The $CoFe_2O_4$@NF electrode measured in 50 °C alkaline solution provided the lowest Tafel slope of 42 mV/dec, as could be expected from the corresponding CV curve in Figure 6a. In fact, such an outstanding kinetic behavior makes it an ideal anode candidate for commercial water splitting systems. Nevertheless, besides the electrochemical performance also the electrochemical durability is a major parameter in the realization of industry-viable electrodes for electrolyzers. For this purpose, we investigated the long-term stability for the $CoFe_2O_4$@NF electrode (3 dips), as illustrated in Figure 6d. Again, bare NF was utilized

for comparison and the stability was assessed by cycling the electrodes 1000 times in 1M KOH (ambient temperature). It can be observed that the $CoFe_2O_4$@NF showed a negligible degradation after continuous 1000 CV cycles, indicating its superior operational stability under alkaline test condition. This was also confirmed by the HRTEM analysis shown in Figure S5 in the SI. As apparent, the NPs remained thinly dispersed and maintained their size after the long-term experiment. There was no obvious aggregation and expansion, thanks to the immobilization effect of the NF scaffold.
Furthermore, as generally known and observable from the long-term behavior of the bare NF in Figure 6d, the bare Ni foam catalyst slightly increases its activity towards OER with time in alkaline solutions due to metallic impurities (e.g. Fe) in the electrolyte which deposit onto the Ni surface during long-term operations and act as co-catalysts.[28] Because such a behavior was not observable in the case of the $CoFe_2O_4$@NF, we can assume that Ni only acts as the scaffold material and the $CoFe_2O_4$ as the active catalyst.
In general, it is also important to determine the active surface area of the catalyst-coated scaffold. For this purpose, we estimated the electrochemical active surface area (ECSA) for the $CoFe_2O_4$@NF (3 dips) in comparison to the ECSA of bare Ni foam. In fact, the ECSA can be estimated from the electrochemical double-layer capacitance (C_{dl}) at the solid/liquid interface.[29] Figure S6a and S6b (SI) present the CV curves of the two electrodes recorded in a non-Faradic potential range under different scan rates. From Figure S6c, it can be deduced that the $CoFe_2O_4$ nanoparticles-coated Ni foam cathode exhibited a higher C_{dl} than bare Ni foam, evidencing a higher active surface area, which was estimated as 80.5 cm^2 for the $CoFe_2O_4$ coated Ni foam and 31.0 cm^2 for the bare Ni foam. This result demonstrates that the synthesized $CoFe_2O_4$@NF could afford a larger number of catalytically active sites and thus an improved OER activity, much higher than that of $CoFe_2O_4$ particles on carbon nanofibers (20.6 cm^2), for instance, and even much higher than that of the commercial RuO_2 catalyst (14.5 cm^2).[15]

2.2.3 Prototype Electrolysis Reactor

The subsequent step consisted in the integration of the optimized large-scale $CoFe_2O_4$@NF electrode in a prototype electrolysis reactor, which was already presented in our previous works.[29-31] As illustrated in Figure 7a, the reactor design allows to work under flow conditions, where the anolyte and catholyte electrolyte solutions are continuously recirculated (by two peristaltic pumps) through the respective compartments, i.e. the anode compartment with the $CoFe_2O_4$@NF and the cathode compartment with a Ti/Pt plate performing the HER. By this design, the flow dynamics of the electrolysis set-up could be significantly enhanced, fostering higher electrochemical activity.[30] Both compartments were separated by a membrane and a gas chromatograph was employed for gaseous product detection. The configuration can even be adapted for the additional integration of photovoltaic devices, as exemplarily shown in Figure 7a for a thin-film silicon solar cell.
The characteristics of the complete reactor device in two-electrode operation are shown in Figure 7b for two different configurations: The first configuration consisted in using a cation-exchange membrane (Nafion ®117) membrane and 1M KOH electrolyte solution in both compartments. In the second configuration, we applied a bipolar membrane (BPM), enabling to operate the electrolysis reactor with two different electrolytes. In this configuration, we applied the 1M KOH (pH = 13.7) for the anolyte to perform the OER and a 1M H_2SO_4 (pH = 0) solution for the catholyte to perform the HER. As can be seen from the linear sweep voltammetry (LSV) curves in Figure 7b, the configuration applying the BPM exhibited a better overall electrolysis behavior than the reactor configuration containing the Nafion membrane. To provide 200 mA and 400 mA, respectively, the BPM

configuration only required 1.51 V and 1.59 V, respectively, whereas in the Nafion configuration the complete electrolyzer cell voltage augmented to 1.60 V and 1.76 V, respectively. The higher observed cell voltage originated from the reduced electrochemical performance of the Ti/Pt cathode in alkaline solution (Nafion configuration) compared to its performance in acid electrolytes (BPM configuration). In Figure S7, the LSV curves of Ti/Pt are shown in 1M KOH and 1M H_2SO_4 electrolyte solution, respectively, evidencing the superior performance in the acidic medium. To simulate real electrolyzer conditions, the overall polarization of the reactor device was also measured at elevated electrolyte temperatures (50 ºC) in the BPM configuration. As expected from the results shown in Figure 6a and Figure S7, the electrochemical performance increased with increasing electrolyte temperature, reaching complete electrolyzer cell voltages of 1.46 V and 1.51 V, respectively, to produce 200 mA and 400 mA, respectively.

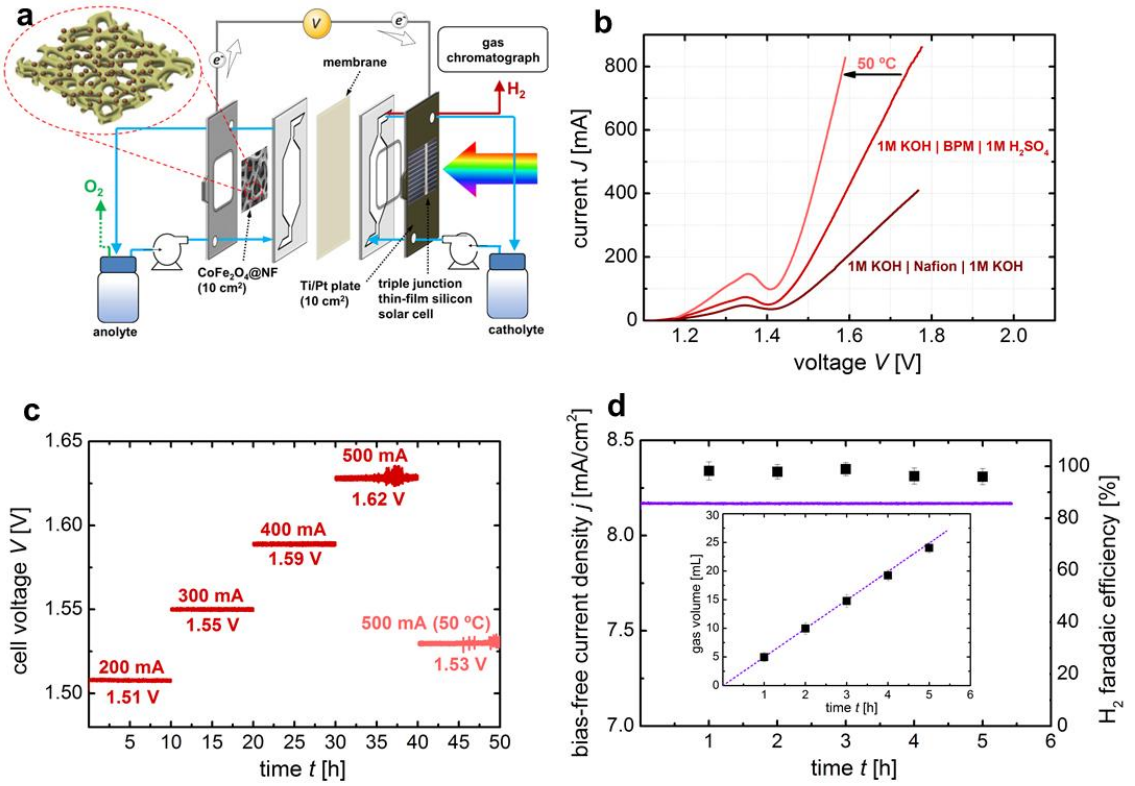

Figure 7. a) Sketch of the experimental prototype reactor used to assess the overall electrolysis performance. The illustration shows the different components, including a schematic illustration of the 3D Ni foam coated with the $CoFe_2O_4$ NPs and the applied triple junction thin-film silicon solar cell (a-Si:H/a-Si:H/µc-Si:H) for the bias-free operation test (see Figure 7d). b) Linear sweep measurements of the $CoFe_2O_4$@NF electrodes (10 cm^2 geometric area) combined with the Ti/Pt cathode (10 cm^2 geometric area) for a configuration containing Nafion and BPM membrane, respectively. The BPM configuration (best performing) was also measured at 50 ºC electrolyte solution (1M KOH). c) Long-term behavior of the electrolysis showing the required cell voltages of the reactor as a function of the applied current (each galvanostatic testing was conducted for ~10 hours with the same electrodes and membrane). d) Bias-free solar water splitting using a triple junction a-Si:H/a-Si:H/µc-Si:H solar cell (as depicted in a)). Left y-axis shows the achieved bias-free current density over the operation time. Right y-axis represents the faradaic efficiency for H_2 production over the operation time. The error bars indicate standard deviations obtained from 3 experimental repeats. The inset shows the calculated gas volume obtained. The dotted purple line shows the theoretical (assuming 100% faradaic efficiency) gas evolution for the measured bias-free current density and the black squares show the experimental values.

Electrochemical durability of the prototype reactor regarding electrolysis operation was assessed by conducting chronoamperometry. In Figure 7c, the electrolyzer cell voltages as a function of the operation time are plotted for different electrolysis currents of 200, 300, 400, and 500 mA, which were applied for 10 hours each. Hence, the prototype electrolyzer was operated for 50 hours with no sign of decay, even not when operated at higher temperatures. In addition to that, the measurement in Figure 7c revealed that the large-scale geometric electrode areas were conducive to high stability achieving industrial relevant currents, along with impressively low electrolyzer cell voltages of 1.62 V and 1.53 V at ambient and elevated temperature, respectively. These values are among the record performance indices for overall water splitting using inexpensive and earth-abundant catalysts. Additionally, the present study assessed their performance also on large-scale electrodes in a prototype electrolyzer. The aspect of process scalability is vital in view of a real-world application, however, has neither been experimentally evidenced, nor sufficiently discussed in previous related studies on OER materials (exemplarily see electrode areas in Table S1 in the SI). Hence, these studies focus on laboratory scale electrodes, neglecting critical issues, which have been addressed in the present study, such as homogeneous coverage of active electrocatalyst on the large-scale scaffold, higher chemical resistivity or cheap processing techniques.

3. Discussion

Given its remarkable activity, the prototype electrolysis reactor can easily be powered by renewable energy sources, such as photovoltaics, to produce (solar) hydrogen, as clean and effective energy carrier. The conversion of solar energy into chemical fuels energy is a promising route for future energy conversion and storage concepts. For this purpose, we electrically attaching a cheap and scalable thin-film silicon solar cell to the prototype reactor, as illustrated in Figure 7a. In particular, a triple junction a-Si:H/a-Si:H/µc-Si:H solar cell was applied, with a photovoltaic conversion efficiency of around 13.4%.[32] The corresponding current density-voltage *(j-V)* curve is shown in Figure S8 in the SI and overlaid with the polarization curve of the electrolyzer device. The crossing point of both *j-V* curves, which can serve as estimation for the bias-free operation current density of the solar-driven electrolyzer, lied in the plateau region of the solar cell characteristics (near the maximum power point) at 1.45 V and 8.2 mA/cm^2. To account for deviations in the assessment of the photovoltaic performance of the complete system, i.e. spectra variations due to diode calibration accuracy, area definition, or temperature variation, for instance, a systematic error of 2 % was suggested.[33] The bias-free measurement of the solar-driven electrolyzer is shown in Figure 7d and provided evidence that the prototype electrolyzer can be powered only by sunlight energy and provided 8.15 ± 0.16 mA/cm^2 current density. The faradaic efficiency for H_2 production was also measured by gas chromatography (Figure 7a) and was found to be close to 100 % over the course of bias-free operation (> 5 hours), as depicted on the right ordinate in Figure 7d. The inset in Figure 7d shows the theoretical and experimentally determined bias-free H_2 gas production over time, proving that H_2 was the only product formed during electrolysis (besides O_2). With these values, a solar-to-hydrogen conversion efficiency of 10.03 ± 0.2 % can be calculated, which is among the record bias-free water splitting efficiencies for thin-film silicon based devices.[32,34]. Overall, this example suggests that the low overpotentials electrolyzer based on the developed $CoFe_2O_4$@NF can match the stringent requirements for high efficient renewable energy conversion and storage at large scale.
In fact, the enhanced OER catalytic activity can be ascribed to the combination of nano-sized active $CoFe_2O_4$ particles with the 3D macroporous structure of the supporting Ni

foam itself, as illustrated in Figure 7a. This marriage resulted in a significantly increased contact area between catalysts and electrolytes and provided a greater amount of active sites where OER could take place (see ECSA estimation in the SI, Figures S6c). Furthermore, the flow cell design of the applied reactor ensured an improved transport of reactants and products.

In general, the coupling of pure academic with engineered systems is urgently needed to mature renewable fuel production processes and open the pathway towards commercial application. This aspect is successfully addressed by the herein proposed system. In addition, the scalable process of the developed $CoFe_2O_4$@NF electrode paired with the adaptability of the presented prototype reactor bears great benefits and cross-fertilization for a number of related catalytic and photovoltaic technologies. Thus, our electrolyzer concept is not limited to small active electrode areas[35,36] or expensive small-scale photovoltaic structures[37] but can be adapted to large scale designs. Nevertheless, from a scientific point of view, further attention should be devoted to investigate earth-abundant and active HER electrodes. The herein applied Ti/Pt plate served as stable and reliable proof-of-concept electrode, but could be replaced by a cathode system, which does not contain rare materials such as Pt. From a more engineering point of view, the evaluation of different approaches to upscale the photovoltaic structures up to the geometric size of the electrochemical active surface areas could be alluring if integrated photoelectrochemical cell (PEC) systems are envisaged. In this "PEC-farm" approach, multiple medium-scaled electrolyzers, i.e. electrolyzers similar to the herein presented prototype (10-100 cm^2 active photovoltaic and electrochemical electrode areas), could operate independently, while the produced fuels of all the electrolyzers would be collected together.[38] The advantageous feature of this concept is that lower photocurrent densities would be required, which would be beneficial regarding lower overpotential losses and thus, eventually higher overall solar-to-fuel efficiencies. In this regard, it is projected by techno-economic models of large scale, centralized solar H_2 production facilities that overpotential losses at high operating current densities are one of the most important factors in reducing the STH efficiency and thus, increasing the cost of H_2.[39,40]

In total, all these examples manifest the high versatility and vast range of applications of the herein presented scalable $CoFe_2O_4$@NF electrode and electrolysis system, respectively.

4 Conclusion

In conclusion, we have presented a simple and scalable colloidal synthesis and coating strategy for the concurrent anchoring of $CoFe_2O_4$ nanoparticles homogeneously on three-dimensional nickel foam. Compared with the single component counterparts (pure $CoFe_2O_4$ and bare Ni foam), the synthesized $CoFe_2O_4$@NF are demonstrated to be an efficient earth-abundant OER electrocatalyst system with ultralow overpotential, large current density, small Tafel slope, and long-term durability in alkaline solution. The improved catalytic performances are believed to originate from the unique synergy between the nano-scaled active $CoFe_2O_4$ catalysts and the highly conductive and high area Ni scaffold. Considering the cost-effectiveness, facile, and reliable fabrication process, and outstanding catalytic performance, the $CoFe_2O_4$@NFs may hold great potential to future energy conversion and storage devices. Moreover, the optimized large-scale $CoFe_2O_4$@NFs (10 cm^2 geometric active area) were integrated in a prototype electrolysis reactor, where currents of 500 mA were achieved with electrolyzer cell voltages of 1.62 V and 1.53 V at ambient and elevated temperatures, respectively, over prolonged operation times. The high activity of the $CoFe_2O_4$@NF based electrolyzer furthermore Importantly, the present versatile synthetic strategy may stimulate future

lines of work, which will be needed to address efficiency improvements and technoeconomical questions while assessing cost competitiveness.

5 Experimental Section

5.1. *Chemicals and Materials*

Cobalt(II) acetylacetonate ($Co(acac)_2$, 97%, Sigma-Aldrich), Iron acetylacetonate ($Fe(acac)_3$, 97% Sigma-Aldrich), oleylamine (OAm, 80–90%, TCI), oleic acid (OAc, Sigma-Aldrich), Nafion (10 wt%, perfluorinated ion-exchange resin, dispersion in water), methanol (anhydrous, 99.8%, Sigma-Aldrich), carbon black (CB, VULCAN XC72), potassium hydroxide (KOH, 85%, Sigma-Aldrich)， tetrafluoroboric acid (HBF_4,48% Gew in H_2O Sigma-Aldrich） and acetonitrile (CH3CN, extra dry, Fisher) were used as received without any further treatment. Chloroform, hexane, acetone, and ethanol were of analytical grade and purchased from various sources. Milli-Q water was obtained from a PURELAB flex from ELGA. An argon-filled glove box was used for storing and handling sensitive chemicals.

5.2. *Synthesis of Colloidal $CoFe_2O_4$ Nanoparticles*

All the syntheses were performed using standard airless techniques, i.e. a vacuum/dry argon gas Schlenk line. $CoFe_2O_4$ NPs were synthesized by loading 1.0 mmol of Fe(acac)3, 1mmol of Co(acac)2, 10 ml OAm and 1.0 ml OAc in a three-neck flask and degassed under vacuum at 80 ºC for 1 hour while being strongly stirred using a magnetic bar. Subsequently, the reaction flask was heated to 230 ºC and maintained for 30 min, while continuously adding nitrogen into the flask. A visible color change was observed immediately (see Figure 1a). The obtained NPs were collected by centrifuging and washing the solid product with acetone and hexane three times. The as-prepared NPs were finally dispersed in hexane with a concentration of 10 mg/mL and stored for further use. NPs were colloidally stable in chloroform for a couple of weeks.

5.3. *Ligand Removal*

In a typical process, 10 mL of $CoFe_2O_4$ NPs dispersion in hexane (10mg/mL) was combined with 10 mL acetonitrile to form a two-phase mixture and then a 1 mL HBF4 solution (48%) was added. The resulting solution was sonicated until the NPs transferred from the upper to the bottom layer. The surface modified NPs were washed with ethanol for three times and dispersed in 10 mL ethanol with a small amount of DMF for further use.

5.4.*Coating of Ni Foam*

Drop casting:
Ni foam was sonicated in acetone, 1M HCl, Milli-Q water, and ethanol respectively. 50 µL of 10mg/mL $CoFe_2O_4$ ethanol solution was dropped on nickel foam and dried in air and subsequently annealed at 400℃ under nitrogen atmosphere.
Dip coating:
Ni foam was sonicated in acetone, 1M HCl, Milli-Q water, and ethanol respectively. In a typical process, clean and dry nickel foam was immersed in 10mg/mL of $CoFe_2O_4$ ethanol solution for 2 seconds and then taken out quickly and dried in air. This process was repeated for 1, 3, 5, and 7times and donated as 1dip, 3 dips, 5 dips, 7dips, respectively. The coated NF were subsequently annealing at 400℃ under nitrogen atmosphere.

5.5. *Characterization*

Structural characterization was carried out by X-ray diffraction (XRD). The samples were scanned from $2\theta = 20°$ to 80° at a rate of 0.02 s^{-1} in Bragg–Brentano geometry. The diffractometer was equipped with a Cu Kα (1.54051 Å) radiation source. The morphology of the as deposited foam-based electrodes was observed using a scanning electron microscope (SEM) and elemental analysis was performed by the same microscope equipped with an X-ray energy dispersive spectrometer (EDS). The samples for transmission electron microscope (TEM) were prepared by scratching the as-prepared $CoFe_2O_4$ powders from the Ni foam substrate, followed by dispersing them in hexane and collecting them on the TEM copper grids. High resolution transmission electron microscopy (HRTEM) images and scanning transmission electron microscopy (STEM) studies were conducted by using an FEI Tecnai F20 field emission gun microscope operated at 200 kV with a point-to-point resolution of 0.19 nm, which is equipped with high angle annular dark field (HAADF) and electron energy loss spectroscopy (EELS) detectors.

The electrochemical performance of the $CoFe_2O_4$@NF towards OER reduction was assessed using a three-electrode set-up. A leak-free Ag/AgCl 3.4 M KCl reference electrode (RE) was assembled in the polytetrafluoroethylene (PTFE) frame of the cell and placed very close to the working electrode surface. The potential was transformed to the reversible hydrogen electrode (RHE) scale: $E\,(V_{RHE}) = E\,(V_{Ag/AgCl}) + 0.0592 \times pH + 0.197$. The data presented for the electrochemical characterization in aqueous solutions in three-electrode configuration do not include compensation for the series resistance of the solution. For the complete electrolyzer characterization, an adapted flow cell set-up (Micro Flow Cell, Electrocell A/S) was employed, schematically depicted in Figure 7a. The flow rates of electrolytes within the flow cell were kept at 20 ml/min. As illustrated in Figure 7a, the electrolyte was directly introduced through the macroporous 3D $CoFe_2O_4$@NF electrode (geometric surface area: 10 cm^2). For details on the cyclic voltammetry (CV) and gas chromatography (GC) regarding the assessment of current-voltage behavior and the faradaic efficiency for gaseous products, respectively, the reader is referred to Ref. 29 and Ref. 30. The electrically attached triple junction thin-film silicon device had an area of 1 cm^2, thus during the photoelectrolysis measurement an area of 1 cm^2 was illuminated. All photoelectrochemical experiments were conducted using a solar simulator equipped with a 150 W xenon lamp. The intensity of the light source was adjusted to match standard AM 1.5G sunlight at 100 mW/cm^2 intensity. The experiments for the full system assembly were carried out in a two-electrode configuration. The faradaic efficiency to H_2 were calculated using the analysis of the outlet gas by gas chromatography (GC) during potentiostatic measurements. Helium (99.999%) was used as the carrier gas. The calibration of peak area vs. gas concentration was used for the molar quantification of each gaseous effluent. The faradaic efficiency was calculated by determining the number of coulombs needed for each product and then dividing by the total charge passed during the time of the GC sampling according to the flow rate.

Acknowledgments

Authors acknowledge funding from Generalitat de Catalunya through the CERCA program, 2017 SGR 1246, 2017 SGR 327 and the Spanish MINECO projects MAT2014-59961, ENE2016-80788-C5-5-R and ENE2017-85087-C3, together with the support from REPSOL, S. A. ICN2 is supported by the Severo Ochoa program from Spanish

MINECO (Grant No. SEV-2017-0706). IREC also acknowledges additional support from the European Regional Development Funds (ERDF, FEDER), (S)TEM part of the present work has been performed in the framework of Universitat Autònoma de Barcelona Materials Science PhD program and the rest in the Nanoscience program of the University of Barcelona. The authors thank S. Moll (IEK-5), M. Biset-Peiró (IREC), and H. Xie (IREC) for their contribution to this work. F.U. acknowledges financial support from MINECO through Juan de la Cierva fellowship (FJCI-2016-29147).V.S. and F.F. (authors from IEK-5) thank the Deutsche Forschungsgemeinschaft (DFG) (Priority Program SPP 1613).

Author contributions

F.U., J. R. M. and A.C. conceived the project and designed the experiments. F.U. carried out the (photo)-electrochemical experiments. R.D. conducted the synthesis and coating of the Ni foam. P.Y.T., R.D. and J.A. conducted the structural and compositional analyses. F.U., R.D. and P.Y.T. interpreted data. F.U. wrote the manuscript. V.S. and F.F. performed and supervised the deposition of the multijunction thin-film silicon solar cells. J.R.M. T.A. and A.C. supervised the proposed and executed research program. All the authors participated in discussions and contributed to editing of the manuscript.

Conflict of Interest

The authors declare no conflict of interest.

6. References

[1] S. B. Walker, U. Mukherjee, M. Fowler, A. Elkamel, *Int. J. Hydrogen Energy* **2016**, *41*, 7717.
[2] Y. Wang, B. Kong, D. Zhao, H. Wang, C. Selomulya, Nano Today **2017**, *15*, 26.
[3] C. C. L. McCrory, S. Jung, I. M. Ferrer, S. M. Chatman, J. C. Peters, T. F. Jaramillo, *J. Am. Chem. Soc*. **2015**, *137*, 4347.
[4] S. Ardo et al., *Energy Environ. Sci.* **2018**, ***11***, 2768.
[5] M. Ball, M. Weeda, Int. J. Hydrogen Energy **2015**, *40*, 7903.
[6] T. Rostrup-Nielsen, *Catalysis Today* **2005**, *106*, 293.
[7] K. Chakrapani, G. Bendt, H. Hajiyani, I. Schwarzrock, T. Lunkenbein, S. Salamon, J. Landers, H. Wende, R. Schlögl, R. Pentcheva, M. Behrens, S. Schulz, *ChemCatChem* **2017**, *9*, 2988.
[8] H. Zhou, F. Yu, Q. Zhu, J. Sun, F. Qin, L. Yu, J. Bao, Y. Yu, S. Chen, Z. Ren, *Energy Environ. Sci.* **2018**, *11*, 2858.
[9] T. Maiyalagan, K. A. Jarvis, S. Therese, P. J. Ferreira, A. Manthiram, *Nat. Comm.* **2014**, *5*, 3949.
[10] M. Tahir, L. Pan, F. Idrees, X. Zhang, L. Wang, J.-J. Zou, Z. L.Wang, *Nano Energy* **2016**, *37*, 136.
[11] M. Li, Y. Xiong, X. Liu, X. Bo, Y. Zhang, C. Han, L. Guo, *Nanoscale* **2015**, *7*, 8920.
[12] A. Kargar, S. Yavuz, T. K. Kim, C.-H. Liu, C. Kuru, C. S. Rustomji, S. Jin, P. R. Bandaru, *ACS Appl. Mater. Interfaces* **2015**, *7*, 17851.
[13] Y. Xu, W. Bian, J. Wu, J.-H. Tian, R. Yang, *Electrochim. Acta* **2015**, *151*, 276.

[14] W. Yan, X. Cao, J. Tian, C. Jin, K. Ke, R. Yang, *Carbon* **2016**, *99*, 195.
[15] T. Li, Y. Lv, J. Su, Y. Wang, Q. Yang, Y.Zhang, J. Zhou, L. Xu, D. Sun, Y. Tang, *Adv. Sci*. **2017**, *4*, 1700226.
[16] X.-F. Lu, L.-F. Gu, J.-W. Wang, J.-X. Wu, P.-Q. Liao, G.-R. Li, *Adv. Mater*. **2017**, *29*, 1604437.
[17] W. Bian, Z. Yang, P. Strasser, R. Yang, *J. Power Sources* **2014**, *250*, 196.
[18] X. Ji, S. Hao, F. Qu, J. Liu, G. Du, A. M. Asiri, L. Chen, X. Sun, *Nanoscale* **2017**, *9*, 7714.
[19] Y.-F. Xu , X.-D. Wang, H.-Y. Chen, D.-B. Kuang, C.-Y. Su, *Adv. Funct. Mater*. **2016**, *26*, 4414.
[20] C. Singh, A. Goyal, S. Singhal, Nanoscale, **2014**, *6*, 7959.
[21] M. Kruk, M. Jaroniec, S. Guan, S. Inagaki, *J. Phys. Chem. B* **2001**, *105*, 681.
[22] H. G. Meier, J. R. Vilche, A. J. Arvía, J. Electroanal. Chem. Interfacial Electrochem. **1982**, *138*, 367.
[23] E. B. Castro, C. A. Gervasi, J. R. Vilche, *J. Appl. Electrochem*. **1998**, *28*, 835.
[24] I. G. Casella, M. Gatta, *J. Electroanal. Chem*. **2002**, *534*, 31.
[25] M. Walter, S. Doswald, F. Krumeich, M. He, R. Widmer, N. P. Stadie, M. V. Kovalenko, *Nanoscale* **2018**, *10*, 3777.
[26] Z. Luo, J. Lu, C. Flox, R. Nafria, A. Genç, J. Arbiol, J. Llorca, M. Ibáñez, J. R. Morante, A. Cabot, *J. Mater. Chem. A* **2016**, *4*, 16706.
[27] S. H. Joo, S. J. Choi, I. Oh, J. Kwak, Z. Liu, O. Terasaki, R. Ryoo, *Nature* **2001**, *412*, 169.
[28] S. Klaus, Y. Cai, M. W. Louie, L. Trotochaud, and Alexis T. Bell, *J. Phys. Chem. C* **2015**, *119*, 7243.
[29] F. Urbain, P. Tang, N. M. Carretero, T. Andreu, J. Arbiol, J. R. Morante, *ACS Appl. Mater. Interfaces* **2018**, *10*, 43650.
[30] F. Urbain, P. Tang, N. M. Carretero, T. Andreu, L. G. Gerling, C. Voz, J. Arbiol, J. R. Morante, *Energy Environ. Sci*. **2017**, *10*, 2256.
[31] E. Irtem, T. Andreu, A. Parra, M. D. Hernández-Alonso, S. García-Rodríguez, J. M. Riesco-García, G. Penelas-Pérez, and J. R. Morante, *J. Mater. Chem. A* **2016**, *4*, 13582.
[32] F. Urbain, V. Smirnov, J.-P. Becker, A. Lambertz, F. Yang, J. Ziegler, B. Kaiser, W. Jaegermann, U. Rau, F. Finger, *Energy Environ. Sci*. **2016**, *9*, 145.
[33] A. Lambertz, F. Finger, R. E. I. Schropp, U. Rau, V. Smirnov, *Prog. Photovolt: Res. Appl.* **2015**, *23*, 939.
[34] C.Trompoukis, A. Abass,J.-W. Schüttauf, T. Bosserez, J. Rongé, J. Lauwaert, J. A. Martens, R. Baets, *Solar Energy Mater. Sol. Cells* **2018**, *182*, 196 .
[35] Y. Tan, H. Wang, P. Liu, Y. Shen, C. Cheng, A. Hirata, T. Fujita, Z. Tang, M. Chen, *Energy Environ. Sci*. **2016**, ***9***, 2257
[36] N. Jiang, B. You, M. Sheng, Y. Sun, *Angew. Chem. Int. Ed*. **2015**, *54*, 6251. [11] M. Q. Yu, Y. H. Li, S. Yang,P. F. Liu, L. F. Pan, L. Zhang, G. Yang, *J. Mater. Chem. A* **2015**, *3*, 14101.
[37] J. Jia, L. C. Seitz, J. D. Benck, Y. Huo, Y. Chen, J. W. Desmond Ng, T. Bilir, J. S. Harris, T. F. Jaramillo, *Nat. Comm*. **2016**, *7*, 13237.
[38] F. Urbain, P. Tang, V. Smirnov, K. Welter, T. Andreu, F. Finger, J. Arbiol, J. R. Morante, ChemSusChem **2019**, accepted manuscript, DOI: 10.1002/cssc.201802845.
[39] B. M. Klahr, D. Peterson, K. Randolph, E. L. Miller, *ECS Trans*. **2017**, *75*, 3.

[40] J. H. Montoya, L. C. Seitz, P. Chakthranont, A. Vojvodic, T. F. Jaramillo, J. K. Nørskov, *Nat. Mater*. **2017**, *16*, 70.